Recent results from experimental studies on laser–plasma coupling in a shock ignition relevant regime

2013 Plasma Phys. Control. Fusion 55 124045

(http://iopscience.iop.org/0741-3335/55/12/124045)

Plasma Phys. Control. Fusion **55** (2013) 124045 (8pp) doi:10.1088/0741-3335/55/12/124045

Recent results from experimental studies on laser–plasma coupling in a shock ignition relevant regime

P Koester[1], L Antonelli[2,3], S Atzeni[4], J Badziak[5], F Baffigi[1], D Batani[3], C A Cecchetti[1], T Chodukowski[5], F Consoli[6], G Cristoforetti[1], R De Angelis[6], G Folpini[7], L A Gizzi[1], Z Kalinowska[5], E Krousky[8], M Kucharik[9], L Labate[1], T Levato[1,2], R Liska[9], G Malka[3], Y Maheut[3], A Marocchino[4], P Nicolai[3], T O'Dell[10], P Parys[5], T Pisarczyk[5], P Raczka[5], O Renner[8], Y J Rhee[11], X Ribeyre[3], M Richetta[2], M Rosinski[5], L Ryc[5], J Skala[8], A Schiavi[4], G Schurtz[3], M Smid[8], C Spindloe[10], J Ullschmied[12], J Wolowski[5] and A Zaras[5]

[1] Intense Laser Irradiation Laboratory, INO-CNR, Pisa, Italy
[2] Dipartimento di Ingegneria Industriale, University of Rome 'Tor Vergata', Rome, Italy
[3] Universite Bordeaux, CNRS, CEA, CELIA (Centre Lasers Intenses et Applications), UMR 5107, F-33405 Talence, France
[4] Dipartimento SBAI, Università di Roma 'La Sapienza' and CNISM, Italy
[5] Institute of Plasma Physics and Laser Microfusion, Warsaw, Poland
[6] Associazione ENEA-Euratom sulla Fusione, Frascati, Italy
[7] Dipartimento di Fisica 'G. Occhialini', University of Milano-Bicocca, Milan, Italy
[8] Institute of Physics, ASCR, Prague, Czech Republic
[9] Czech Technical University, FNSPE, Prague, Czech Republic
[10] Scitech Precision, Rutherford Appleton Laboratory, Chilton, Didcot, Oxon, UK
[11] Nuclear Data Center, KAERI, Korea
[12] Institute of Plasma Physics ASCR, Prague, Czech Republic

E-mail: petra.koester@ino.it

Received 17 July 2013, in final form 9 October 2013
Published 28 November 2013
Online at stacks.iop.org/PPCF/55/124045

Abstract

Shock ignition (SI) is an appealing approach in the inertial confinement scenario for the ignition and burn of a pre-compressed fusion pellet. In this scheme, a strong converging shock is launched by laser irradiation at an intensity $I\lambda^2 > 10^{15}$ W cm^{-2} μm^2 at the end of the compression phase. In this intensity regime, laser–plasma interactions are characterized by the onset of a variety of instabilities, including stimulated Raman scattering, Brillouin scattering and the two plasmon decay, accompanied by the generation of a population of fast electrons. The effect of the fast electrons on the efficiency of the shock wave production is investigated in a series of dedicated experiments at the Prague Asterix Laser Facility (PALS).

We study the laser–plasma coupling in a SI relevant regime in a planar geometry by creating an extended preformed plasma with a laser beam at $\sim 7 \times 10^{13}$ W cm^{-2} (250 ps, 1315 nm). A strong shock is launched by irradiation with a second laser beam at intensities in the range 10^{15}–10^{16} W cm^{-2} (250 ps, 438 nm) at various delays with respect to the first beam. The pre-plasma is characterized using x-ray spectroscopy, ion diagnostics and interferometry. Spectroscopy and calorimetry of the backscattered radiation is performed in the spectral range 250–850 nm, including (3/2)ω, ω and ω/2 emission. The fast electron production is characterized through spectroscopy and imaging of the $K\alpha$ emission. Information on the shock pressure is obtained using shock breakout chronometry and measurements of the craters produced by the shock in a massive target.

Preliminary results show that the backscattered energy is in the range 3–15%, mainly due to backscattered light at the laser wavelength (438 nm), which increases with increasing the delay between the two laser beams. The values of the peak shock pressures inferred from the shock breakout times are lower than expected from 2D numerical simulations. The same simulations reveal that the 2D effects play a major role in these experiments, with the laser spot size comparable with the distance between critical and ablation layers.

(Some figures may appear in colour only in the online journal)

1. Introduction

The shock ignition (SI) scheme is a promising approach to inertial confinement fusion (ICF) due to the relative simplicity and potential high gain [1–3]. In the SI scheme, the compression phase is separated from the ignition phase. In the first phase, the thermonuclear fusion capsule is compressed by irradiation with nanosecond laser beams at an intensity below 10^{15} W cm^{-2}. In the second phase, a high-intensity (10^{15}–10^{16} W cm^{-2}) laser pulse is used to launch a strong shock of several hundreds of Mbar, generating ignition conditions in a central hot spot.

In the intensity regime accessed in the ignition phase, the laser–plasma interaction is characterized by the onset of parametric instabilities, including stimulated Brillouin scattering (SBS), stimulated Raman scattering (SRS) and the two plasmon decay (TPD). Laser plasma interactions have been extensively studied in recent decades for laser intensities above 10^{14} W cm^{-2}. Strong reflectivity (up to several tens of percent) due to the occurence of parametric instabilities was observed during the irradiation of low-Z planar targets with infrared laser light at intensities around 10^{16} W cm^{-2} [4]. On the other hand, in an experiment with similar irradiation conditions, the back-reflected energy was found to saturate at a level of 10% [5]. Experiments with shorter (UV) laser wavelength irradiation were also performed for intensities up to 10^{15} W cm^{-2}, showing backscattered energies at a level below 10% [6–8]. The instabilities can give rise to an increased reflection of the laser light (SBS and SRS) and the generation of longitudinal electron plasma waves (SRS and TPD) and the subsequent production of suprathermal electrons. The effect of these suprathermal electrons on the shock wave efficiency is currently under investigation. The moderately energetic electrons (<100 keV) are produced at the end of the compression phase when the large areal density might prevent preheat due to the penetration of the fast electrons into the pre-compressed fuel. Moreover, theoretical and numerical studies have shown that the suprathermal electrons might enhance shock drive performance through enhancement of the ablation pressure and symmetrization of the shock pressure front [1, 9–11].

Recently, the first experiments were performed to study laser–plasma interactions and shock propagation simultaneously [12, 13]. In experiments in a spherical geometry, an enhancement of the neutron yield was observed for a properly timed high-intensity laser beam [12, 14]. Experiments in a planar geometry showed modest backreflection (<15%) for laser irradiation at intensities up to 10^{15} W cm^{-2} and a wavelength of 532 nm [13]. Here we report on an experimental study in planar geometry for laser irradiation at intensities in the range 10^{15}–10^{16} W cm^{-2}. The experimental study aims at investigating laser–plasma instabilities and suprathermal electron production in an extended plasma in the intensity regime 10^{15}–10^{16} W cm^{-2} and to study their effect on the generation of a strong shock.

2. Experiment

The experiment was performed at the Prague Asterix Laser Facility (PALS) laser facility. A schematic view of the experimental setup is shown in figure 1. An auxiliary beam at the fundamental wavelength $\lambda = 1.3\,\mu$m with a duration of 250 ps irradiated the target at an angle of 30° from target normal in the vertical direction. The intensity was 7×10^{13} W cm^{-2} in a nearly flat top 900 μm diameter focal spot to create an extended plasma. The main laser beam was converted to 3ω ($\lambda = 438$ nm, pulse duration 250 ps) and focused at normal incidence to intensities on the target, up to 9×10^{15} W cm^{-2} in a Gaussian focal spot with full width half maximum (FWHM) = 100 μm to create a strong shock. Both beams were equipped with phase plates to generate homogeneous irradiation of the target surface. On a few shots, the phase plate on the main beam was removed to reach higher intensities (up to 3×10^{16} W cm^{-2}) in a focal spot with diameter ~60 μm. However, in this case, the laser intensity distribution was far from being homogeneous. The delay between the two laser beams was varied in the range 0–1200 ps. Time measurements refer to the peak of the laser pulses, thus delay 0 refers to both laser beams overlapping in time. The intensity of the main laser pulse was varied in the range 10^{15}–10^{16} W cm^{-2} by varying the laser pulse energy, whereas pulse duration and focal spot size were kept fixed throughout the experiment.

Two types of targets were used in the experiment. The so-called thin multilayer targets consisted of a plastic layer of 25 μm thickness on the laser-irradiated side. This layer contained Cl (C_8H_7Cl, parylene-C) for x-ray spectroscopic measurements. The second layer, a 5 μm thick Cu layer, was used for the detection of suprathermal electrons through $K\alpha$ measurements. The 25 μm thick Al layer at the rear side of the target was used for shock chronometry. In some targets, an additional 10 μm Al step allowed us to infer the shock velocity at the rear side of the target. The second type of targets, the so-called thick targets, consisted of the same plastic layer of either 25 or 40 μm thickness on the laser-irradiated side. The second layer consisted of a few mm thick Cu, used for $K\alpha$ measurements and determination of the shock parameters through crater measurements.

From a diagnostic point of view, the density of the plasma created by the auxiliary beam was characterized by a 3-frame optical interferometric system employing a frequency-doubled ($\lambda = 657$ nm) probe beam. The plasma temperature was measured using a high resolution x-ray spectrometer based on a spherically bent mica crystal. The spectrometer was set to reflect the spectral range between 3.5 and 4.5 Å including line emission from H-like, He-like and Li-like Cl ions.

The backscattered laser light was characterized through spectroscopy and calorimetry of the radiation collected by the focusing lens ($f/2$). In addition, $(3/2)\omega$ emission (at 292 nm) of the main laser frequency, which is not transmitted by the focusing lens, was collected by means of an optical system inside the vacuum chamber and sent to a spectrometer with the use of an optical fiber. A set of calorimeters placed inside the vacuum chamber monitored the light scattered outside the lens cone.

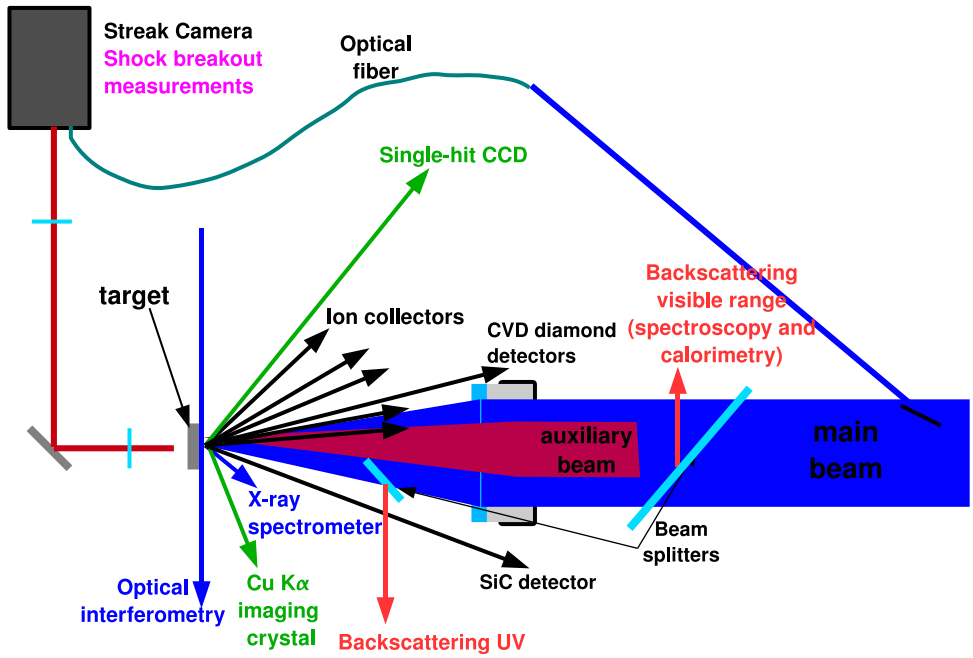

Figure 1. Schematic view of the experimental setup (top view).

For the suprathermal electron detection, $K\alpha$ measurements were performed. The flux of $K\alpha$ photons originating from the target Cu layer was measured using a CCD working in the single-hit regime [26]. The size of the Cu $K\alpha$ emitting region was measured through 2D imaging by means of a spherically bent quartz (2 1 1) crystal, set up as a monochromator in imaging mode [15].

In addition, ion measurements were performed using ion collectors, an SiC detector and diamond detectors. Eight ion collectors were placed at different angles between the laser propagation direction and the direction along the target surface for the measurement of slow ions. Fast ions were detected by means of the SiC detector placed at an angle of 30° with respect to the laser propagation direction.

The shock pressure was inferred using shock breakout chronometry for the thin targets and through crater measurements in the thick targets. For the shock breakout measurements, the self-emission from the rear target side was imaged by an optical system on the entrance slit of a streak camera. The shock breakout time was measured with respect to a so-called fiducial: a small portion of the main laser beam with a known delay with respect to the time when the main beam reaches the target. The measured shock breakout times were compared to results obtained from simulations with the 2D hydro-code DUED [16] to infer the shock pressure. For the thick targets, the volume and depth of the craters produced in the Cu layer were measured. The interaction of the laser with the thick targets was hydrodynamically modeled by the 2D code PALE (Prague ALE) [17]. The code includes ALE (arbitrary Lagrangian Eulerian) hydrodynamics, flux limited heat conductivity with the Spitzer–Härm conductivity coefficient and ray-tracing laser absorption through inverse bremsstrahlung and resonance mechanisms. The shock generated in the plastic by the laser hits the Cu surface and creates a crater in the Cu layer. By the simulated crater, we understand the volume of evaporated and melted Cu (phase change enthalpies are not included in the equation of state). The maximum of this volume reached in the simulation is considered as the simulated crater volume.

3. Results

In the following, an overview of the experimental results is given. This section is divided into four parts. In the first part, the pre-plasma characterization is presented. In the second part, experimental results from measurements regarding parametric instabilities are shown, followed by the description of the suprathermal electron characterization. Finally, the results from the shock parameter measurements are presented.

3.1. Pre-plasma characterization

The pre-plasma density profile was measured at different times with respect to the interaction of the auxiliary laser beam with the target. In figure 2, a graph of the pre-plasma extension measured at an electron density of $10^{19}\,\mathrm{cm}^{-3}$ is shown as a function of the expansion time. Time zero corresponds to the peak of the auxiliary beam on target. As can be seen from the graph in figure 2, the pre-plasma thickness increases almost linearly with time. At the maximum, the experimental delay between auxiliary and main laser beam of 1200 ps the plasma size is 0.7 mm. As higher density regions are not accessible to the interferometric measurements, the electron density scalelength L_n at higher densities is estimated from hydrodynamic simulations. At $n_c/10$ ($n_c/4$), where n_c indicates the critical density, the scalelength increases from 20 μm (4 μm) at 250 ps to 65 μm (25 μm) at 1150 ps after the peak of the auxiliary beam.

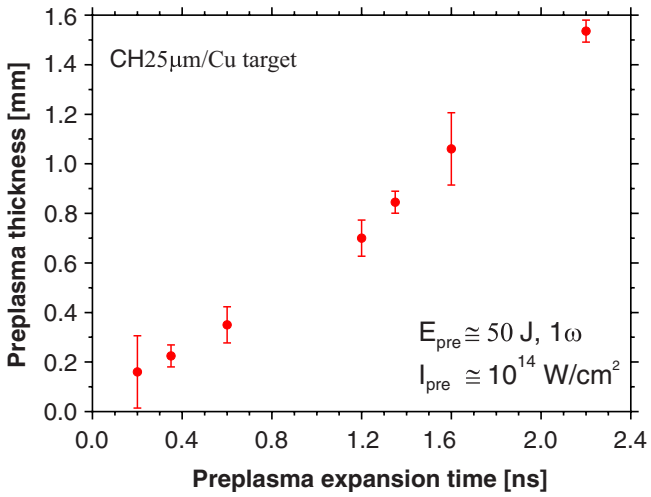

Figure 2. The longitudinal plasma size measured at $n_e = 10^{19}$ cm^{-3} as a function of expansion time.

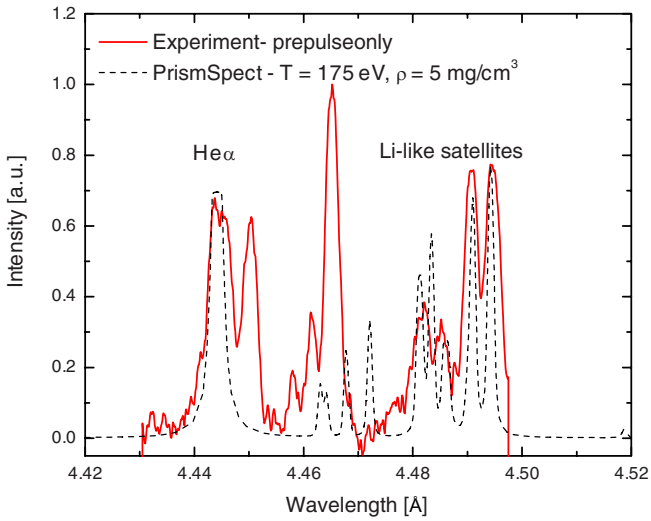

Figure 3. Experimental Cl line emission spectrum obtained from the irradiation of a parylene-C (C_8H_7Cl) target with the auxiliary beam only (solid red line). The spectrum calculated with the PrismSpect code for a temperature of 175 eV is also shown (dashed black line).

In figure 3, the x-ray emission spectrum in the range between 4.42 and 4.52 Å, obtained from the irradiation of the target with the auxiliary laser beam only, is displayed (solid red line). In the spectrum, the Cl Heα line and satellite lines are clearly visible. The experimental data is compared to a spectrum calculated with the PrismSpect code [18], which is also shown in the graph of figure 3 (dashed black line). Best agreement with the experimental spectrum is obtained for a plasma temperature of 175 eV. This temperature is much lower than the temperature in the plasma corona of a pre-compressed fuel capsule (2–4 keV for ignition designs using a plastic ablator [19]) as envisaged in the SI scheme.

3.2. Parametric instabilities

In order to get information about the amount of energy backscattered due to parametric instabilities, calorimetry of the backscattered light was performed in two spectral regions in a narrow range around the main laser frequency and above 550 nm. For the data shots with the phase plate inserted on the main laser beam, the overall backscattered energy in the lens cone is measured to be below 10% of the laser energy and is dominated by backscattered light at the laser frequency, which includes both Brillouin scattered light and laser light back-reflected at the critical density surface. The Raman backscattered energy is very low, of the order of 0.1% of the laser energy. Both signals increase with increasing delay between the two laser beams as expected, since the instabilities become more important with increasing plasma scalelength. The results obtained from the irradiation without the phase plate on the main laser beam show similar trends for the backscattered energy, with the difference that the overall backscattered energy increases by a factor of about 2. This may partly be due to the increased laser intensity due to the smaller focal spot size. In addition, nonlinear interaction due to the non-uniformity of the laser intensity profile in the focal spot is more important for irradiation without the phase plate. In fact, the experimental results obtained without the phase plate show higher shot-to-shot fluctuations, indicating that nonlinear interaction occurs.

Spectroscopy of the Raman signal was also performed in the experiment. In figures 4(*b*)–(*e*), typical spectra obtained for delays of the main laser beam with respect to the auxiliary beam between 0 and 1200 ps are shown. A spectrum obtained from the irradiation of the target with the main beam is also shown (figure 4(*a*)). As can be seen from the graphs, the spectral width of the Raman signal increases from 10 to 50 nm for increasing delays. Also, the long wavelength cut-off increases with increasing delay from about 700 to 740 nm. In the graph in figure 4(*f*), the dependence of the plasma density of the SRS as a function of the SRS emission wavelength is shown. According to the plot, the maximum observed long wavelength cut-offs correspond to the SRS emission at electron densities of $0.135\,n_c$ and $0.175\,n_c$ respectively, where n_c indicates the critical density for the main beam laser frequency.

(3/2)ω emission, a signature of TPD, was also detected in the experiment, thus showing that the laser light reached a quarter of the critical density. A typical spectrum around the wavelength $\lambda = 292$ nm, corresponding to (3/2)ω of the main laser frequency, is shown in figure 5. The spectrum shows the typical structure of a signal originating from TPD, with the red and blue components of the emission due to coupling of the blue and red shifted electron plasma waves with the main laser wavelength.

Both the SRS and TPD can lead to the generation of a population of suprathermal electrons. However, a strong correlation was found between the SRS backscattered energy and the $K\alpha$ photon number, as shown in figure 6, supporting the conclusion that SRS is mainly responsible for the generation of suprathermal electrons.

3.3. Suprathermal electrons

The presence of suprathermal electrons was detected through $K\alpha$ measurements with a CCD working in single-photon regime and a spherically bent quartz crystal set to reflect

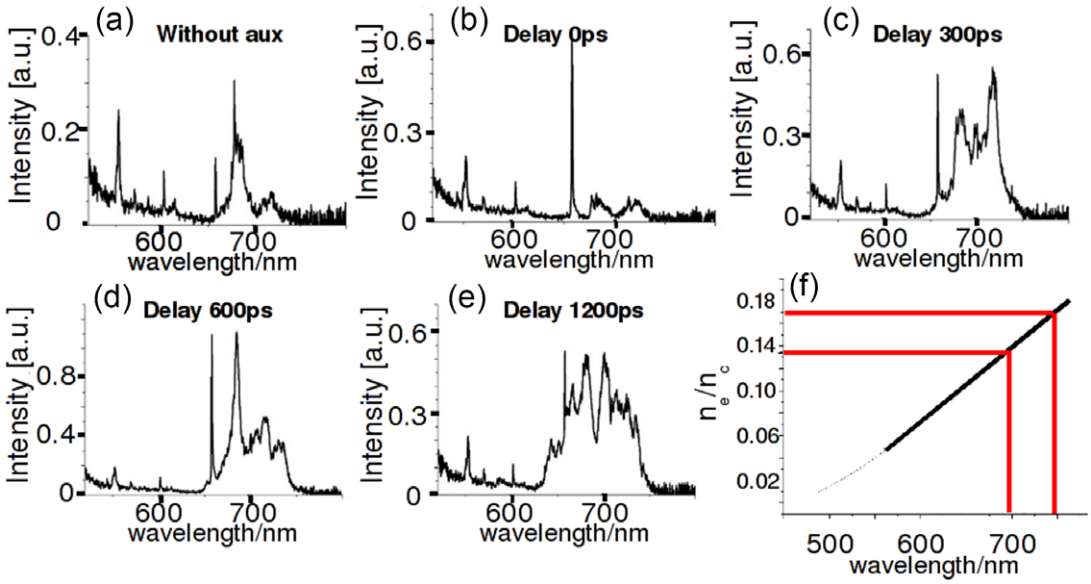

Figure 4. Typical SRS spectra obtained from the irradiation of the multilayer target with the main beam only (*a*) and for different delays in the range from 0 and 1200 ps between the auxiliary and the main beam (*b*)–(*e*). The calculated dependence of the density at which SRS occurs as a function of the SRS emission wavelength is also shown in (*f*).

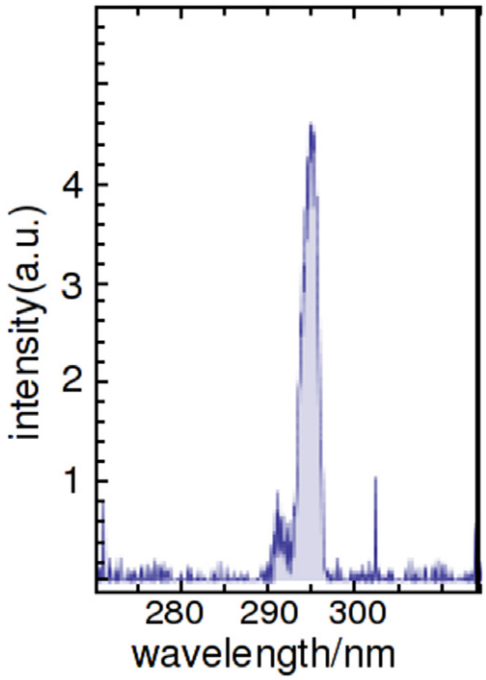

Figure 5. A typical spectrum around (3/2)ω of the main laser frequency, corresponding to a wavelength $\lambda = 292$ nm.

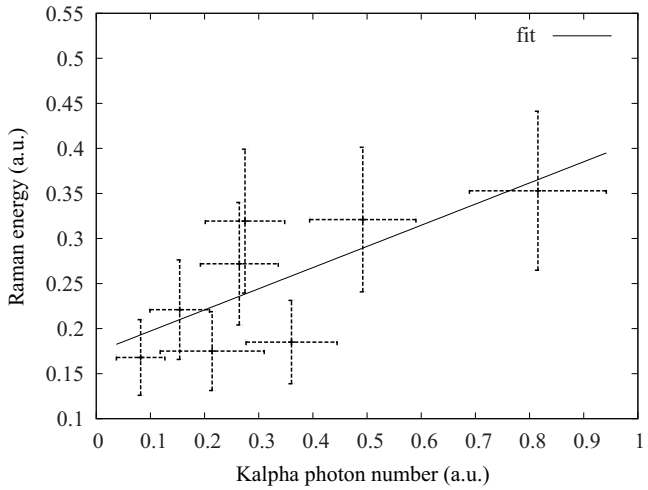

Figure 6. Correlation between the backscattered energy due to SRS and the $K\alpha$ photon number measured with the CCD working in the single photon regime.

Cu $K\alpha$ line emission in an imaging configuration. A lineout of a typical image of the Cu $K\alpha$ emission spot is displayed in the graph in figure 7 together with a Gaussian fit. The lineout was taken in the vertical direction, which is not affected by distortions of the image due to the observation angle of the crystal with respect to the target normal. The measured FWHM $K\alpha$ spot size is of the order of $\sim$150 μm for all data shots, consistent with a divergent propagation of the low energy suprathermal electrons as expected. In fact, taking into account a propagation distance of the fast electrons of about 100 μm as inferred from simulations, the divergence half-angle turns out to be 37°.

The $K\alpha$ photon flux was measured with the CCD and the $K\alpha$ imaging crystal. The Cu $K\alpha$ photon number emitted in 4π was calculated from the acquired data assuming isotropic emission. The $K\alpha$ photon number increases with increasing laser energy as expected and lies in the range 2×10^9–2×10^{10}. The resulting conversion efficiency from laser energy to $K\alpha$ photons is independent of the laser intensity within the experimental error ($\sim$25%) and shot-to-shot fluctuations and is of the order of 10^{-7}. These results are consistent with the results obtained from the measurements with the crystal imager.

The penetration depth of the suprathermal electrons was inferred from measurements of the $K\alpha$ photon flux obtained

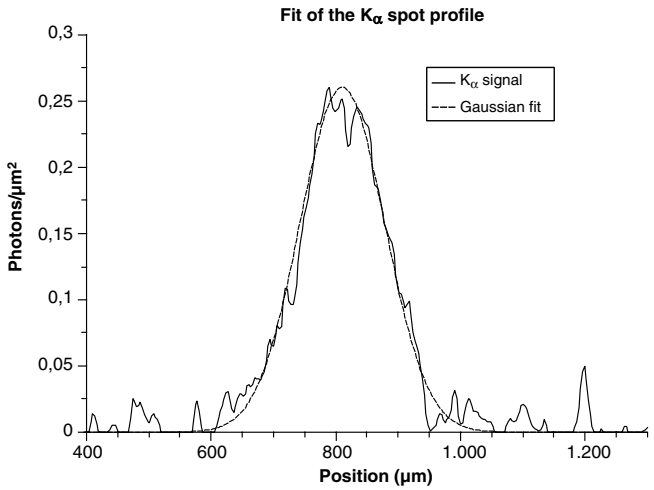

Figure 7. Vertical lineout of a typical image of the Cu $K\alpha$ spot together with a Gaussian fit. The best fit is obtained for a diameter (FWHM) of 151 μm.

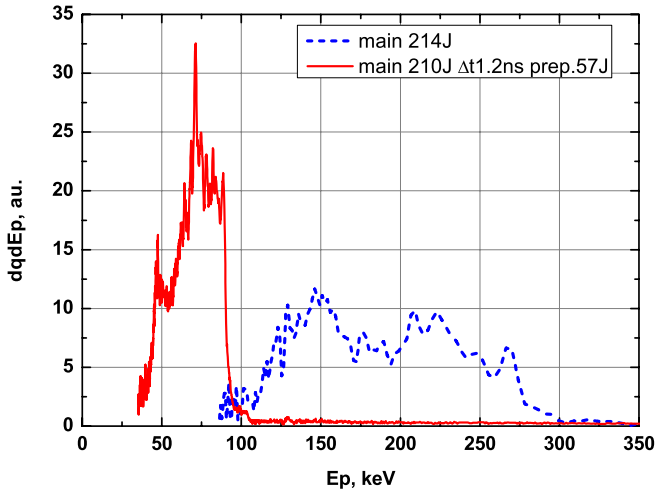

Figure 8. Energy spectra of fast ions (protons) emitted from a plasma produced by irradiation with the main pulse only (blue dashed line) and for irradiation with both beams at a delay of 1200 ps (red continuous line).

from the irradiation of thick targets with different thicknesses of the plastic layer. The measured flux as a function of the plastic layer thickness was fitted with an exponential function $N(x) = a+b\exp^{-x/L}$, where N, x and L indicate the measured photon number, the plastic layer thickness and the penetration depth and a and b are free fitting parameters. The best fit was obtained for a penetration depth $L = 27 \pm 8\,\mu$m. From a comparison of the result with the electron stopping range in mylar, as given by the ESTAR database [20], the electron energy is estimated to be $\sim$50 $\pm$ 10 keV. The assumption of a monoenergetic electron beam instead of a more realistic electron energy distribution does not alter the resulting electron energy estimate significantly. In fact, the major contribution to the $K\alpha$ emission originates from a $\sim$10 μm thick surface layer of the thick Cu layer due to reabsorption of the $K\alpha$ emission originating from greater depths. Therefore, the high energy tail of the suprathermal electron distribution function does not alter significantly the $K\alpha$ photon flux with respect to a monoenergetic electron beam. From the total $K\alpha$ photon flux and assuming a single-temperature electron distribution function with a mean energy of 50 keV, the conversion efficiency into suprathermal electrons is estimated to be of the order of $0.1 \pm 0.02\%$.

The energy of the suprathermal electrons can also be estimated from the measurements of fast ions by means of the SiC detector. In the graph in figure 8, typical energy spectra of the fast ions (protons) are displayed for two different irradiation conditions, i.e. for irradiation with the main beam only (blue dashed line) and for irradiation with both beams for a delay of 1200 ps (red continuous line). As can be seen in the graph, the two spectra differ significantly for the two irradiation conditions. In the absence of a pre-plasma, that is for irradiation with the main beam only, fast ion energies up to $\sim$270 keV are observed, whereas in the presence of an extended pre-plasma, the highest observed ion energy is $\sim$90 keV. In both cases, the total charge of the fast ions is below 1% of the total charge of thermal ions. Since the fast ions are driven by suprathermal electrons, these findings suggest that the suprathermal electron generation is dominated by different absorption mechanisms in the two conditions. In fact, it is expected that resonance absorption plays a significant role in the absence of a pre-plasma, whereas suprathermal electron generation through TPD and/or SRS are expected to dominate in the long scalelength plasma. The hot electron temperature T_e was inferred from the fast ion (proton) measurements using the relation $E_i/A = aT_e$, where a is the number of the value somewhere between 2 and 12 depending on the model [21, 22], E_i is the mean ion energy and A is the atomic number. For the estimate of T_e, we used the empirical value $a = 4.5$ [21, 22] determined from a comparison of the LASNEX code calculations with a set of experimental data from various laboratories [21]. Using this value, for the proton energy spectra presented in figure 8, we arrive at $T_e \sim 50$ keV for the case when the pre-plasma is absent (the main pulse only) and $T_e \sim 20$ keV for the largest experimental delay between the two laser beams (1200 ps). These values are roughly in agreement with the results from $K\alpha$ measurements.

3.4. Shock measurements

The shock parameters were measured through shock chronometry for the thin targets and through crater measurements for the thick targets. In the graph in figure 9, the shock breakout times are shown as a function of laser intensity. As the measured shock breakout times were found to be independent of the delay between the two laser beams, data for all delays are shown in the same graph. Shock breakout times, as obtained from simulations with the 2D hydro-code DUED [16], for laser intensities divided by a factor of 2 are also shown in the graph (green triangles); the corresponding peak pressure in the plastic layer, before shock intensification by impedance mismatch, is indicated. As can be seen in the graph, the shock breakout times obtained from the irradiation with the phase plate inserted on the main beam (black circles) follow the scaling law of stationary shocks in the classical regime $t \propto I^{-1/3}$. The data obtained from irradiation

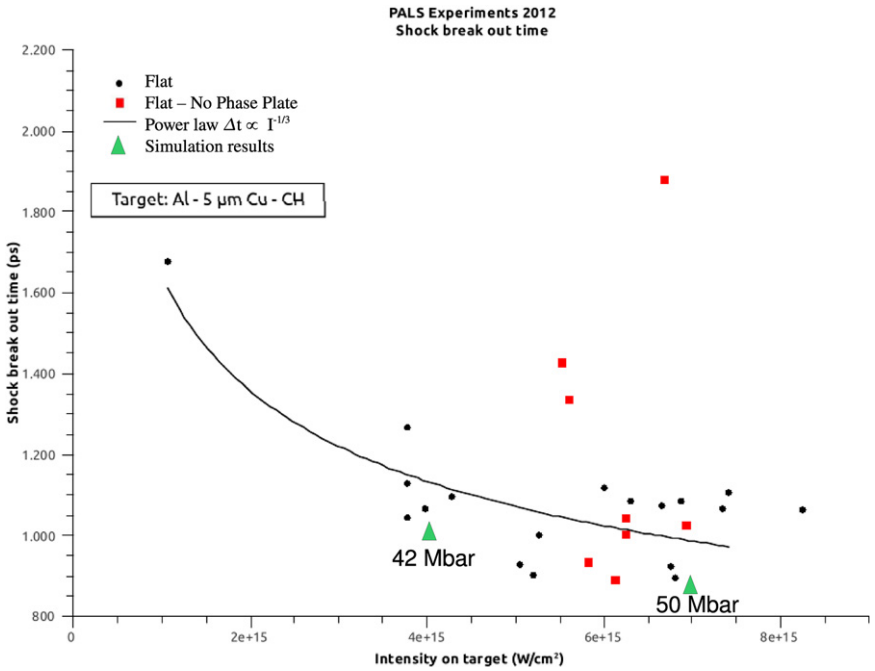

Figure 9. Shock breakout times at the rear of the target as a function of laser energy for irradiation of the target with the phase plate inserted on the main beam (black circles) and for irradiation without phase plate (red squares). Shock breakout times as obtained from simulations with the 2D hydro-code DUED shown for laser intensities divided by 2 are also shown (green triangles). A fit with the scaling law $t \propto I^{-1/3}$ for stationary shocks in the classical regime is also shown.

without the phase plate (red squares) show much higher shot-to-shot fluctuations as also observed in the backscattering measurements, indicating nonlinear interaction due to the strong non-uniformity of the laser intensity distribution in the focal spot. The peak pressure generated in the plastic layer inferred from simulations are much lower than those expected from 1D scaling laws for the ablative regime. In fact, for a laser intensity of 7×10^{15} W cm^{-2} and a laser wavelength of 438 nm, a peak pressure of about 230 Mbar is expected [23, 24], whereas the peak pressure inferred from simulations for the measured shock breakout times at an intensity of 7×10^{15} W cm^{-2} is 50 Mbar. The simulations show that 2D effects occur for the experimental focal spot size, which lower the peak pressure by a factor of ∼2. Nevertheless, the laser intensity has to be lowered by a factor of 2 in the simulations in order to recover the experimental data. The origin of this discrepancy is currently under investigation and is discussed in detail in [25]. A possible explanation concerns larger than simulated energy losses due to light refracted at large angles in the plasma corona. In fact, total laser absorption was not measured in the experiment. On the other hand, deviation from the ablative regime might be expected at high laser intensities, as indicated in recent theoretical works [11, 24]. Further experimental investigation will be needed to clarify these issues.

In the graph in figure 10, the measured volume of craters obtained from the irradiation of thick targets is shown as a function of the laser energy. The crater volume and thus the shock pressure increases with increasing laser energy as expected. The pressure was inferred from the crater measurements through a comparison of the experimental data with simulation results from the 2D PALE code. The

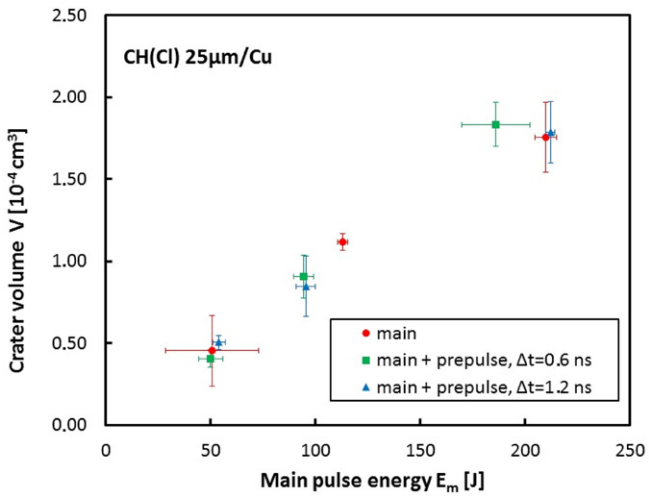

Figure 10. The volume of craters produced in the Cu layer of the thick targets as a function of laser energy. Data for different irradiation conditions is displayed: irradiation with the main beam only (red circles), with both beams for a delay of 600 ps (green squares) and of 1200 ps (blue triangles).

maximum inferred pressure for a laser intensity of 9×10^{15} W cm^{-2} was about 100 Mbar with an uncertainty of about 20%. Considering shot-to-shot fluctuations, scaling with intensity and the experimental errors (10–15%), this result is consistent with the pressure inferred from shock breakout measurements.

Data with the main laser beam was obtained for delays in the range of 0–1200 ps. In figure 10, the measured crater volumes are displayed for irradiation with the main beam only and for two different delays between the auxiliary and the main

beam (600 and 1200 ps). As can be seen from the graph, the crater volume and thus the shock pressure is independent of the pre-plasma extension within the experimental error. The same result is obtained from shock breakout measurements on the thin targets. In fact, although the backscattered energy increases with increasing pre-plasma size, the level of backscattered energy is low (<10%) for all delays and does not have a significant effect on the generated shock pressure.

4. Conclusions

An experiment in SI relevant conditions was performed with the laser beam at $3\,\omega$ ($\lambda = 438$ nm) in a planar geometry. The experimental results show a low level of backscattered radiation (<10%) mainly due to SBS. These results are consistent with experiments performed at lower intensity [6–8]. Similar levels of backscattered energy were also observed in recent experiments in a planar geometry [13], whereas much higher levels of backscattered energy were observed in experiments in spherical geometry [12]. The conversion efficiency into kinetic energy of suprathermal electrons was inferred to be well below 1% and the experimental results indicate that the suprathermal electrons are predominantly generated through the SRS process. The mean energy of the suprathermal electron population was estimated to be ~50 keV. The backscattered signal increases with increasing the pre-plasma size as expected. Nevertheless, the overall low level of backscattered light and suprathermal electron generation is consistent with the fact that the shock breakout time and the crater volume, and thus the shock pressure, is found to be independent of the pre-plasma extension within the experimental error. The shock pressure inferred from our measurements is in the range 60–100 Mbar for the highest laser intensities. Although the measured low level of parametric instabilities in our experimental conditions is an encouraging result for the SI scheme, care should be taken, as the preplasma temperature and scalelength are significantly lower than in SI conditions.

Acknowledgments

We would like to acknowledge financial support from the LASERLAB-EUROPE Access to Research Infrastructure activity within the EC's seventh Framework Program (grant agreement no 284464), the National Centre for Science (NCN), Poland under the grant no 2012/04/M/ST2/00452) and the Italian MIUR project PRIN 2009FCC9MS. We also acknowledge the support of HiPER project and Preparatory Phase Funding Agencies (EC, MSMT and SFTC). The work was also supported by the Czech Ministry of Education, Youth and Sports, projects LC528 and LM2010014. SciTech Precision and Rutherford Appleton Laboratory Target Fabrication Group supplied targets. Finally, we thank the technical staff of PALS for help in running the experiments.

References

[1] Betti R *et al* 2007 *Phys. Rev. Lett.* **98** 155001
[2] Atzeni S 2009 *Plasma Phys. Control. Fusion* **51** 124029
[3] Ribeyre X *et al* 2009 *Plasma Phys. Control. Fusion* **51** 015013
[4] Ripin B H *et al* 1977 *Phys. Rev. Lett.* **39** 611
[5] Goldman L M *et al* 1973 *Phys. Rev. Lett.* **31** 1184
[6] Tanaka K *et al* 1984 *Phys. Fluids* **27** 2960
[7] Tanaka K *et al* 1985 *Phys. Fluids* **28** 2910
[8] Regan S P *et al* 1999 *Phys. Plasmas* **6** 2072
[9] Betti R *et al* 2008 *J. Phys.: Conf. Ser.* **112** 022024
[10] Perkins L J *et al* 2009 *Phys. Rev. Lett.* **103** 045004
[11] Guskov S *et al* 2012 *Phys. Rev. Lett.* **109** 255004
[12] Theobald W *et al* 2008 *Phys. Plasmas* **15** 056306
[13] Baton S *et al* 2012 *Phys. Rev. Lett.* **108** 195002
[14] Theobald W *et al* 2009 *Plasma Phys. Control. Fusion* **51** 124052
[15] Koch J A *et al* 2003 *Rev. Sci. Instrum.* **74** 2130
[16] Atzeni S *et al* 2005 *Comput. Phys. Commun.* **169** 153
[17] Liska R *et al* 2011 *Finite Volumes for Complex Applications* VI, *Problems and Perspectives* vol 2 ed J Fort *et al* (Berlin: Springer) pp 57–73
[18] MacFarlane J J *et al* 2007 *High Energy Density Phys.* **3** 181
[19] Anderson K S *et al* 2013 *Phys. Plasmas* **20** 056312
[20] Estar database: http://physics.nist.gov/PhysRefData/Star/Text/ESTAR.html
[21] Gitomer S J *et al* 1986 *Phys. Fluids* **29** 2679
[22] Wilks S C *et al* 2001 *Phys. Plasmas* **8** 542
[23] Manheimer W M *et al* 1982 *Phys. Fluids* **25** 1644
[24] Bell A R and Tzoufras M 2011 *Plasma Phys. Control. Fusion* **53** 045010
[25] Batani D *et al* 2012 *J. Phys.: Conf. Ser.* **399** 012005
[26] Labate L *et al* 2012 *Rev. Sci. Instrum.* **83** 103504